Research Article Vol. 33, No. 1 / 13 Jan 2025 / Optics Express 717
Optics EXPRESS

Robust broadband ptychography algorithms for high-harmonic soft X-ray supercontinua

BENJAMIN SHEARER,[1,*] HENRY KAPTEYN,[1,2] IONA BINNIE,[1] NICHOLAS W. JENKINS,[1] AND MARGARET MURNANE[1]

[1]Department of Physics, University of Colorado, 2000 Colorado Ave., Boulder, Colorado 80309, USA
[2]Kapteyn-Murnane Laboratories, Inc., 4775 Walnut Street, #102, Boulder, Colorado 80301, USA
[*]besh5711@colorado.edu

Abstract: We demonstrate PaCMAN, a ptychography algorithm that can reconstruct high quality images with broadband illumination sources while being robust to shot, detector, and parasitic noise. We extend prior monochromatization work to improve accuracy, especially for discrete spectra, and also demonstrate how PaCMAN can be converted into Ms. PaCMAN, a multi-spectral variant that outperforms multi-spectral ePIE. When comparing speed-optimized ePIE and PaCMAN, we achieve high reconstruction quality in 4x less time, and when they are dose-optimized, we achieve high reconstruction quality in 1.5-2x less dose. These algorithms will enable rapid sub-10 nm imaging with table-top soft X-ray high harmonic supercontinua, advance attosecond coherent diffractive imaging, and reduce the dose needed to image radiation sensitive materials.

1. Introduction

Coherent beams of extreme ultraviolet (EUV) and soft x-ray (SXR) light can now be produced using tabletop high harmonic (HHG) sources as well as high brightness synchrotron and XFEL sources. When combined with coherent diffractive imaging (CDI), it is finally possible to image with sub-wavelength spatial resolution at short wavelengths, and to achieve transverse and axial resolutions on the order of 10 nm and 0.1 nm, respectively [1,2].

Despite tremendous improvements in HHG, synchrotron, and XFEL sources, there are still several factors that limit attainable resolution. Partial spatial coherence limited resolution for older third-generation synchrotrons, but is no longer a limiting factor in diffraction-limited storage rings [3] and is not an issue for HHG sources that are well phase matched [4]. However, parasitic scattering from beamline optics or sample mounting can introduce artifacts on the detectors that are spatially incoherent with respect to the illumination [1,5]. Reconstructing images with diffraction patterns that include parasitic scattering will introduce high frequency ripple artifacts in the image, or can even prevent convergence altogether. The most common approach to address partial spatial coherence has been the inclusion of multiple probe/object modes [6] based on a decomposition of the mutual coherence function. Another method based on the Alternating Direction Method of Multipliers (ADMM) incorporates frame-independent scattering [5].

Another limitation to high fidelity diffractive imaging is associated with quasi-monochromatic or broadband sources, which can span 12 octaves of bandwidth in the soft X-ray region for HHG sources [7,8]. Broad bandwidths radially blur the diffraction patterns, thus corrupting high resolution data at the edges of the patterns. In addition, the probe profile and sample transmission may change significantly over the wavelength range of the illumination, especially near absorption edges. These challenges are commonly addressed by filtering the spectrum using monochromators or other optics that select a narrow portion of the spectrum, effectively throwing away part of the spectrum [1,9]. More efficient algorithms that can use broadband spectra can both improve the usable flux of the source and enable femtosecond or attosecond time resolution spectro-ptychography [10–12].

#541675 https://doi.org/10.1364/OE.541675
Journal © 2025 Received 10 Sep 2024; revised 25 Nov 2024; accepted 5 Dec 2024; published 7 Jan 2025

Optics EXPRESS

One solution to broadband illumination is to implement a multi-wavelength algorithm that solves for multiple wavelength dependent probes and objects, similar to the mixed state approach for spatial coherence [11,13,14]. Multi-wavelength algorithms are particularly useful for reconstructing discrete spectra from a HHG comb [15] or for atto-CDI near absorption edges [11]. They also enable wavefront sensing and characterization of the source [16]. Multi-wavelength algorithms have been demonstrated with ePIE-like updates [11,13] and difference map-like updates [17]. One downside of multi-wavelength algorithms is they have significantly higher data demands than monochromatic algorithms: for example, in [13], an overlap of 90% was used to reconstruct three discrete wavelengths, while in [11], an overlap of 94% was used to reconstruct 17 wavelengths in a continuous spectrum. For context, a scan at a moderate overlap of 70% has 25x less data than a scan at 94%.

One alternative to multi-wavelength algorithms is to monochromatize the diffraction patterns using a measured continuous spectrum, allowing the reconstruction of a single object/probe using standard algorithms like ePIE [10,18,19]. The spectrum can be measured with a spectrometer or solved using a pinhole-filter setup, wherein a quasi-monochromatic diffraction pattern is acquired and used to solve for the full broadband diffraction pattern [20]. Monochromatization algorithms assume the object and probe are wavelength independent, which can be a good approximation for low fractional bandwidths away from absorption edges and for certain experimental setups. Since monochromatization makes stronger assumptions about the diffraction patterns than multi-wavelength algorithms, it does not require extremely high probe overlaps (extra redundant data) or numbers of iterations to converge to an image. This makes monochromatization a promising method for expanding the usable flux from future SXR HHG sources [8].

Lastly, shot and detector noise can limit resolution. Shot noise follows a Poisson distribution and is negligible at high fluxes, while detector noise can be approximated as flux-independent Gaussian distribution [5]. For radiation sensitive materials like catalysts, polymers, resists, and biological cells, we must limit dose to prevent extensive sample damage, which can make Poisson noise a limitation. The standard method for accounting for Poisson noise is through a maximum likelihood model [21], which can be integrated into different optimizers like ADMM [5,22,23].

To date, an algorithm that integrates broadband illumination, spatial coherence, parasitic scattering, and shot/detector noise in the reconstruction has not been demonstrated. The multi-wavelength SPIRE algorithm accommodates partial spatial coherence and broad bandwidths, but does not model noise or parasitic scattering [11]. ADP accommodates parasitic scattering and noise, but not broadband illumination [5]. Recently, several algorithm packages were published, including the multi-language PtyLab [24] and the MATLAB-based PtychoShelves [25]. While these packages provide a wide variety of useful tools for ptychography, neither include a general ADMM framework with background subtraction or numerical monochromatization.

Here, we demonstrate a method that monochromatizes the diffraction patterns and solves for the object and probe through an ADMM framework that compensates for Poisson and parasitic noise. We call this algorithm PaCMAN, which stands for "Partial Coherence and Monochromatization Algorithm with Noise". First, we verify the base PaCMAN algorithm on experimental monochromatic x-ray magnetic circular dichroism data (XMCD) from the COSMIC beamline. Then, we demonstrate an improved monochromatization procedure that significantly reduces the error for discrete spectra and high flux continuous spectra. We compare PaCMAN to standard ePIE [26] at different fluxes through simulations and find that it improves reconstruction quality at all fluxes. Furthermore, when holding the flux constant and changing the probe overlap, PaCMAN can achieve lower dose than ePIE. Finally, we demonstrate that PaCMAN can be adapted into a multi-wavelength algorithm that we call "Multi-spectral, Partial Coherence Mitigating Algorithm with Noise" (Ms. PaCMAN) that exceeds the reconstruction quality of state-of-the-art algorithms in the presence of artifacts. These algorithms will expand the usable flux from SXR HHG supercontinua [27] and push the resolution to sub-10 nm for

Optics EXPRESS

radiation sensitive samples, as well as enable atto-CDI at lower doses. To facilitate this, we make our MATLAB implementation of the code freely available.

2. Theory

2.1. Definitions

Consider a standard ptychography setup with a $N \times N$ pixel detector in the far field. The probe p illuminates a part of the full object o_j, where $j \in [1, J]$ is an index for one of the J scan positions. The full object is given by the $M \times M$ matrix O. We also define a position-dependent probe P_j embedded in a matrix of zeros to be same size as O.

2.2. Monochromatization

If we assume that the object's complex transmission does not change over the bandwidth of the source, the broadband diffraction pattern $b(x, y)$ will be equal to the incoherent sum (or integral) of the dilated intensities $m(x, y)$ weighted by the power spectrum $S(\lambda)$:

$$b(x, y) = \int \frac{1}{\lambda^2} S(\lambda) m\left(\frac{\lambda_0}{\lambda} x, \frac{\lambda_0}{\lambda} y\right) d\lambda. \tag{1}$$

Here, we choose λ_0 to be the center wavelength, which is the wavelength that defines the pixel size in the object plane. By expressing b and m as $N^2 \times 1$ vectors, we can rewrite this integral as

$$b = Cm, \tag{2}$$

where the $N^2 \times N^2$ transformation matrix C is calculated once per spectrum by mapping each pixel in the detector to multiple pixels from the dilated grids of each wavelength in the spectrum [10].

To accurately replicate a continuous spectrum, the scaling between wavelength λ and $\lambda + \delta\lambda$ should be much less than a pixel at the edge of the diffraction pattern [28]. This condition is given by

$$\frac{\lambda}{\delta\lambda} \gg \frac{N}{2}. \tag{3}$$

For Gaussian spectra with an intensity full-width half-maximum of $\Delta\lambda = f\lambda$ with relative bandwidth f, the spectral width that we need to sample is at least $2\Delta\lambda$, which is equivalent to truncating where $S(\lambda \pm \Delta\lambda)$ is 0.06 that of the center wavelength. Solving Eq. (3) for M, the total number of samples required, gives

$$M \gg fN. \tag{4}$$

Thus, sampling is linear in bandwidth and in detector pixel dimension. For $f = 0.05$ (5% bandwidth) and $N = 256$, we get $M \gg 12.8$, while $f = 0.5$ (50% bandwidth) and $N = 256$ gives $M \gg 128$.

To retrieve m, we must solve $m = C^{-1}b$ for each diffraction pattern. Without noise, this can be solved exactly to machine precision. In practice, there is always a small amount of noise, even at very high fluxes. An iterative method called the Conjugate Gradient Least Squares method (CGLS) was applied in previous work due to its robustness to noise [10,18]. However, CGLS is valid for symmetric matrices only, and while C approaches the (symmetric) identity matrix in the monochromatic limit, it increasingly deviates from symmetry when the spectrum is itself asymmetric. To accommodate non-symmetric C while remaining robust to noise, we test a biconjugate gradient stabilized method (BiCGSTAB) [29]. The number of iterations for CGLS and BiCGSTAB in our study is picked automatically as the iteration that minimizes the norm of $b - Cm$, which ranges from zero iterations when b is very noisy to dozens of iterations when b has very low noise. We note that a recent paper implemented the BiCGSTAB algorithm for the

Optics EXPRESS

same inversion, finding similar improvement with the computational spectrometer approach to measuring the spectrum compared to CGLS implemented with a physical spectrometer ([19], see Fig. S3 in supplementary information of reference to compare optimal images).

2.3. Mixed-state model

The j^{th} far-field diffraction pattern for a partially coherent beam can be modeled as the sum of the intensities of L relevant modes that can each have their own probe and object [6]:

$$I_j^{(pc)} = \sum_{l=1}^{L} |\mathcal{F}\{P_{lj} O_{lj}\}|^2. \tag{5}$$

This mixed-state model can account for both partial spatial coherence [6] and partial temporal coherence [11,13], serving as the basis of multi-wavelength algorithms. We will adopt this model to account for spatial coherence for the basic PaCMAN model and temporal coherence in the multi-wavelength variant.

2.4. Alternating direction method of multipliers

For monochromatic, partially spatially coherent illumination, the measured diffraction patterns I_j with Poisson noise, structured noise ϕ, and additive white Gaussian noise with standard deviation σ are given by

$$I_j = \text{Poiss}[I_j^{(pc)} + \phi] + \text{AWGN}_j. \tag{6}$$

Following [5], we can formulate a maximum-likelihood estimate for Poisson noise using the mixed-state model Eq. (5) as

$$\mathcal{G}(z, \mu) = \frac{1}{2} \sum_j \left[\sum_{l=1}^{L} |z_{lj}|^2 + \mu_j^2 - I_j \ln \left(\sum_{l=1}^{L} |z_{lj}|^2 + \mu_j^2 \right) \right] \tag{7}$$

with the corresponding minimization problem

$$\min_{P,O,\mu,z,\sigma} \mathcal{G}(z, \mu) \text{ such that } z_{lj} - \Psi_{lj} = 0 \;\&\; \mu_j - \bar{\mu} = 0, \tag{8}$$

where Ψ is the diffracted wave at the detector plane with a corresponding auxiliary variable z, and μ is an auxiliary variables representing the combined effects of the Gaussian and parasitic noise, with a corresponding mean of $\bar{\mu}$.

The augmented Lagrangian for this minimization is

$$\begin{aligned} \mathcal{L}(P, O, z_l, \sigma_l, \Lambda_l, \bar{\Lambda}, \mu) = \mathcal{G}(z, \mu) &+ r \sum_{l=1}^{L} \sum_j \Re\langle \Lambda_{lj}, z_{lj} - \Psi_{lj} \rangle + r \sum_j \langle \bar{\Lambda}, \mu_j - \bar{\mu} \rangle \\ &+ \frac{r}{2} \sum_{l=1}^{L} \sum_j \left\| \Lambda_{lj}, z_{lj} - \Psi_{lj} \right\|^2 + \frac{r}{2} \sum_j \left\| \mu_j - \bar{\mu} \right\|^2, \end{aligned} \tag{9}$$

where $\langle \cdot, \cdot \rangle$ denotes an inner product and $\| \cdot \|$ denotes the L2 norm. Minimizing Eq. (9) with respect to each of its variables gives an iterative ptychographic algorithm. The derivation is a straightforward extrapolation from the work conducted in [5], and so we refer to this work for details.

Optics EXPRESS

2.5. PaCMAN algorithms

We begin by initializing $z_{lj}^1 = \mathcal{F}\{P_l^1 O_j^1\}$ and the multipliers Λ_{lj}^1 to zeros. The step-size r controls the relative weighting of the Fourier modulus update, with $r = 0$ using only the measured modulus for the update (equivalent to difference map without a noise model [23]) and $r>0$ using both the measured modulus and reconstructed modulus to make the update (Eq. (15)). The object is initialized as ones, while the probe is initialized as a uniform intensity within its support. Additional states ($l>1$) are initialized based on prior information and whether they are temporal states or spatial modes. For each iteration $n = 1...N$, we perform the following:

(1) Define a temporary variable $\bar{z}_{lj}$, which represents an approximate exit wave from the sample:

$$\bar{z}_{lj} = \mathcal{F}^{-1}\left\{z_{lj}^n + \Lambda_{lj}^n\right\}. \tag{10}$$

(2) Update the probe for each state

$$p_l^{n+1} = \frac{p_l^n + \sum_j (o_{lj}^n)^* \bar{z}_{lj}^n}{1 + \sum_j |o_{lj}^n|^2}. \tag{11}$$

(3) Update the object for each state

$$O_l^{n+1} = \frac{O_l^n + \sum_j (P_{lj}^{n+1})^* \bar{z}_{lj}^n}{1 + \sum_j |P_{lj}^{n+1}|^2}. \tag{12}$$

(4) Calculate intermediate variables

$$\Psi_{lj}^{n+1} = \mathcal{F}\{p_l^{n+1} o_{lj}^{n+1}\}, \tag{13}$$

$$X_j = \sqrt{\sum_l |\Psi_{lj}^{n+1} - \Lambda_{lj}^n|^2 + |\bar{\mu} - \bar{\Lambda}_j^n|^2}, \tag{14}$$

$$\rho_j = \frac{rX_j + \sqrt{r^2 X_j^2 + 4(1+r)I_j}}{2(1+r)}. \tag{15}$$

(5) Update z, μ, and the mean $\bar{\mu}$

$$z_{lj}^{n+1} = \rho_j(\Psi_{lj}^{n+1} - \Lambda_{lj}^n)/X_j, \tag{16}$$

$$\mu_j^{n+1} = \rho_j(\bar{\mu} - \bar{\Lambda}_j^n)/X_j, \tag{17}$$

$$\bar{\mu}^{n+1} = \frac{1}{J}\sum_j \mu_j^{n+1}. \tag{18}$$

(6) Update Lagrange multipliers

$$\Lambda_{lj}^{n+1} = \Lambda_{lj}^n + z_{lj}^{n+1} - \Psi_{lj}^{n+1}, \tag{19}$$

$$\bar{\Lambda}_j^{n+1} = \bar{\Lambda}_j^n + \mu_j^{n+1} - \bar{\mu}^{n+1}. \tag{20}$$

Optics EXPRESS

Note that μ and $\bar{\mu}$ would always be zeros in this case. At some iteration $n = N_{\text{pc}}$, we can re-initialize the average background to be the square root of the average difference between the noisy incoherent patterns and the diffraction patterns reconstructed from the probe and its gradients:

$$\bar{\mu}^{n+1} = \sqrt{\max\left\{0, \frac{1}{J}\sum_j \left(I_j - \sum_l |\Psi_{lj}^{n+1}|^2\right)\right\}}. \tag{21}$$

Empirically, choosing N_{pc} to be between 5-20 seems to yield the best results, as it allows for accurate background retrieval with a decent probe/object guess. For PaCMAN, the monochromatization step occurs before the iterations begin, and the only states propagating are spatial modes. For Ms. PaCMAN, we require wavelength-dependent temporal modes, but can use spatial modes as well. The algorithm outlined by Eqs. (10) – (21) is the same for either version.

3. Experiment

First, we test the base algorithm on near-monochromatic x-ray magnetic circular dichroism (XMCD) data from the COSMIC beamline at ALS. The sample, shown in Fig. 1(a), is a thin Fe/Gd film with fiducial holes milled out for ease of alignment. To generate XMCD images with magnetic contrast, we subtract the optical densities found from the ptychographic reconstructions for left and right circularly polarized light. We acquired three tilt series of data to perform vector ptycho-tomography, but limit the discussion here to two datasets—one good and one bad—with different angles in the same tilt series. The primary difference between the datasets is the size of the parasitic scattering region in the diffraction patterns (Fig. 1(b)): the bad dataset acquired at a different angle has a larger parasitic scattering region that extends closer to the center. We ran ePIE and PaCMAN using the unaltered diffraction patterns and 300 iterations, with a probe initialized by the probe reconstructed at the beamline and set to update after iteration 10. For

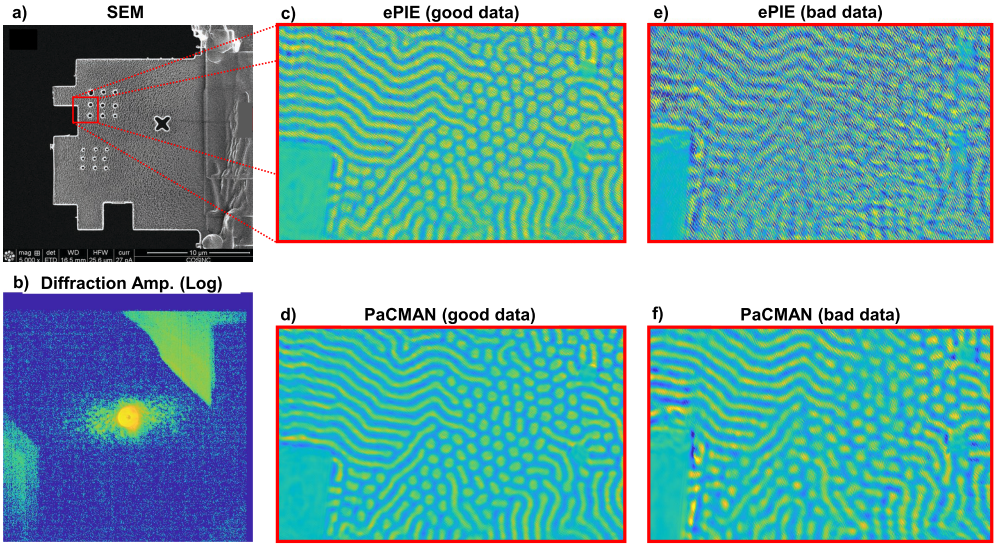

Fig. 1. Experimental XMCD reconstructions. a) SEM image of the sample. b) Representative diffraction amplitude at the detector on a log scale. c-d) XMCD reconstructions for a good dataset. e-f) XMCD reconstructions for a bad dataset. All XMCD reconstructions are plotted on the same color scale.

Optics EXPRESS

ePIE, we set $\beta_{obj} = \beta_{prb} = 1$ and reduced them to 0.5 halfway through the simulations, while for PaCMAN we set $N_{pc} = 20$ and $r = 0.6$. No additional spatial modes were included.

The XMCD reconstructions for ePIE and PaCMAN are shown in Fig. 1(c-f). For the good dataset, the magnetic textures are well reconstructed by both algorithms. However, upon close inspection the ePIE reconstruction has significant ripple artifacts whereas the PaCMAN reconstruction does not. This is due to parasitic scattering, which adds high frequency noise to the reconstructions. For the bad dataset, only PaCMAN achieves decent reconstruction quality, whereas the textures are barely recognizable in the ePIE reconstructions. Thus, the base PaCMAN algorithm works very well even in the presence of noise and artifacts, which is particularly important in ptycho-tomography where the parasitic scattering region can become significant at large tilt angles.

4. Simulations

4.1. Methods

For our simulations, we use a 200×200 pixel object and 64×64 pixel probe embedded in a 256×256 matrix of zeroes to have the same pixel dimensions as the detector. The object and probe are shown in Fig. 2. The object transmission ranges from 0.5 to 1, which results in the diffraction patterns having a photon flux that ranges from 0.264 and 0.995 times the flux incident on the sample, with a mean of 0.696. Unless otherwise noted, we used a moderate probe overlap of 0.7, measured as the linear distance offset [30]. Random offsets of 20% were applied to the probe positions to prevent raster pathology. The center wavelength used was 4.13 nm (300 eV) and the distance between the sample and detector was 5 cm. The effective detector pixel size is 40 μm, yielding a pixel size of about 19 nm in the object plane.

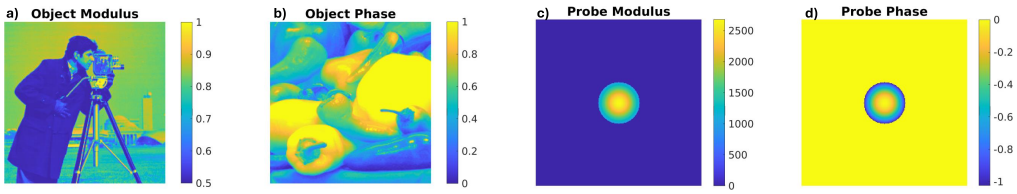

Fig. 2. Object and probe used for the simulations. The object modulus is "cameraman" and the object phase (in radians) is "peppers" (from MATLAB demo images). The probe phase (in radians) and amplitude is a Gaussian with a hard aperture at the 1/e intensity.

To create the broadband diffraction patterns, we dilated the diffraction patterns of the center wavelength (shown in Fig. 3(a)), multiplied them by the appropriate spectral weights, and added them up incoherently to get Fig. 3(b). For the continuous spectra in this study, we used a Gaussian spectrum comprised of 257 wavelengths, which satisfies Eq. (4). The resultant broadband pattern loses much of the speckle contrast of the monochromatic pattern. Monochromatization restores the speckle contrast near the center of the diffraction pattern (Fig. 3(c)).

After creating the broadband patterns, we corrupt the pattern with parasitic scattering (Fig. 3(c)), modelled as a triangular region with a small, constant amplitude in the upper right corner of the diffraction patterns. This type of corruption is fairly common in synchrotrons or table-top experiments, limiting the performance of conventional phase retrieval algorithms [1,5]. Finally, after forming the broadband pattern and corrupting it, we add Gaussian detector noise and Poissonian shot noise.

Optics EXPRESS

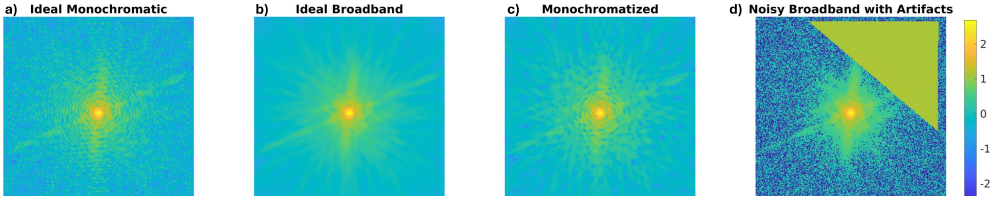

Fig. 3. Sample diffraction pattern amplitudes. a) is the ideal monochromatic amplitude, b) is the ideal broadband amplitude at 20% bandwidth, c) is the ideal broadband amplitude after numerical monochromatization, and d) is the broadband pattern with Poisson noise at a flux of 10^7 photons, Gaussian detector noise, and a triangular parasitic scattering region.

To quantitatively evaluate image quality, we use a normalized root-mean-square error (NRMSE), calculated as

$$\mathrm{NRMSE} = \sqrt{\frac{\frac{1}{N}\sum_{x,y}(|O_{rec}(x,y)| - |O_{exa}(x,y)|)^2}{\frac{1}{N}\sum_{x,y}|O_{exa}(x,y)|^2}}, \tag{22}$$

where the sums over x, y indicate summing each pixel within a region of interest consisting of N pixels.

Unless noted otherwise, we used 200 iterations for all algorithms. For ePIE, we set $\beta_{\mathrm{obj}} = \beta_{\mathrm{prb}} = 0.7$, and halved this halfway through the iterations to improve convergence. For PaCMAN, we set $N_{\mathrm{pc}} = 20$ and $r = 0.4$. The object is initialized as ones, while the probe is initialized as a uniform intensity within its support, which is then updated starting at iteration $N_{\mathrm{prb}} = 5$.

4.2. Varying bandwidth to test monochromatization

We first compare standard ePIE to ePIE with CGLS and BiCGSTAB monochromatization to gauge the effectiveness of the three different algorithms at dealing with continuous and discrete spectra. We set the flux incident on the sample to 10^{10} photons, so Poisson noise is low. No other noise or artifacts were included.

First, we consider continuous Gaussian spectra with bandwidths ranging from 1% to 50%. The reconstructed objects are shown in Fig. 4(i). Without monochromatization, the reconstructions look nearly exact up to a bandwidth of 5%, but degrade significantly beyond about 10% (Fig. 4(ia)). With monochromatization, the reconstructions look nearly exact up to a bandwidth of 20%, but degrade significantly beyond this (Fig. 4(ib-c)). By calculating the NRMSE from 1% to 50%, we see that the error increases linearly with bandwidth (Fig. 4(id)), approaching zero in the monochromatic limit. Monochromatization reduces error at all bandwidths, even at 1%. Compared to CGLS, BiCGSTAB provides greater improvement, especially at larger bandwidths, and achieves the same NRMSE as standard ePIE at more than twice the bandwidth.

Next, we created a discrete spectrum comprised of three wavelengths separated by the bandwidth (i.e. for a 50% bandwidth, we have 0.5λ, λ, and 1.5λ). The spectral weights were set to [2/7, 4/7, 1/7]. The noiseless results are shown in Fig. 4(ii). We can see that CGLS and BiCGSTAB provide comparable improvement below 10%. However, CGLS becomes significantly worse beyond 15% and exceeds the error of ePIE after 25%. BiCGSTAB on the other maintains an error well below 0.01 regardless of bandwidth, returning an image that appears identical to the exact object.

4.3. Varying flux to test noise robustness

To gauge the robustness of PaCMAN, we compare the full PaCMAN algorithm to that of ePIE in the presence of noise and artifacts at different fluxes for continuous and discrete spectra. For both ePIE and PaCMAN, the triangular region of parasitic noise was set to zero. Since the accuracy

Optics EXPRESS

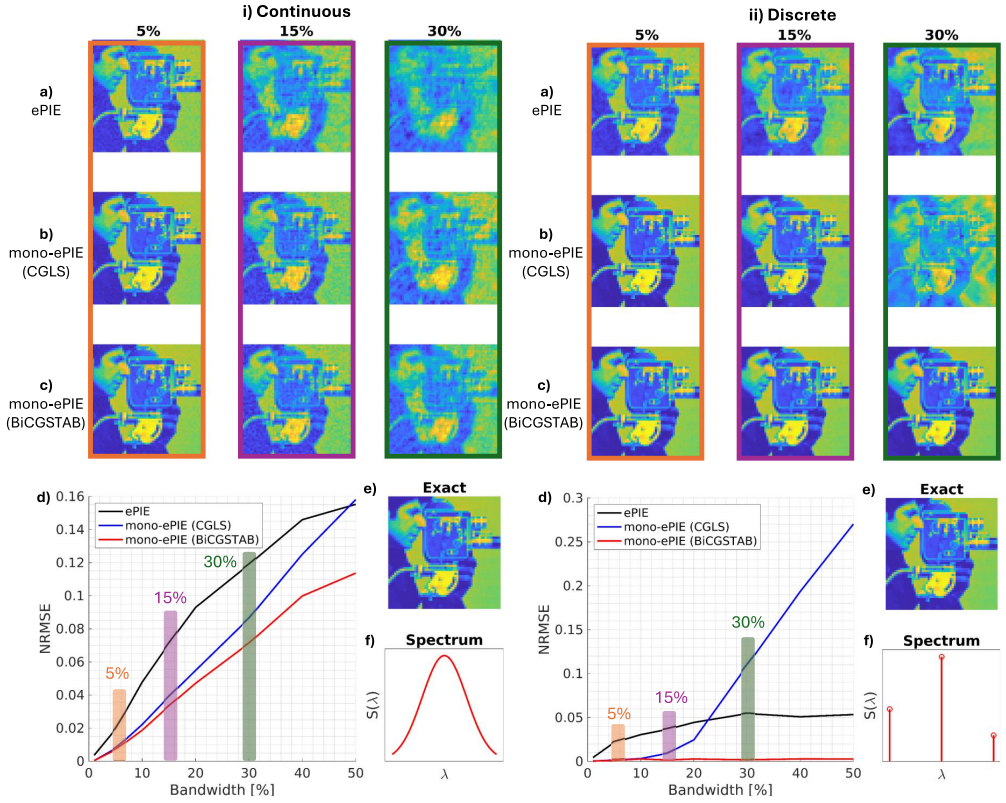

Fig. 4. Reconstructed object modulus as a function of bandwidth for i) a continuous Gaussian spectra and ii) discrete three-wavelength spectra. The images are a) ePIE without monochromatization, b) monochromatized ePIE using CGLS, and c) monochromatized ePIE using BiCGSTAB. d) The NRMSE is plotted as a function of bandwidth, with the shaded regions corresponding to a-c. e) The exact object modulus for reference. f) The spectrum used.

of the monochromatization is sensitive to noise, we tested the base PaCMAN algorithm with and without monochromatization. We test both CGLS and BiCGSTAB to see how noise affects each monochromatization algorithm.

First, we consider a Gaussian spectrum with a bandwidth of 20%. The results are shown in Fig. 5(i). For all fluxes, PaCMAN without monochromatization has superior reconstruction quality, as shown in Fig. 5(ia-b)) and confirmed by the the NRMSE plot in Fig. 5(ic). For fluxes below 10^7, monochromatization increases rather than decreases error. Between 10^7 and 10^9, CGLS has slightly better performance than BiCGSTAB, while in the high flux limit BiCGSTAB has slightly better performance than CGLS, as demonstrated previously in Fig. 4(id). Despite noise, artifacts, a large bandwidth, and a low-moderate probe overlap, PaCMAN with monochromatization can still achieve fairly good reconstruction quality (Fig. 5(ic), flux of 10^9). These results indicate that we can achieve roughly an order of magnitude reduction in dose using PaCMAN rather than ePIE by reducing photon count at fixed probe overlap.

Next, we used the same three-wavelength discrete spectrum as before with a wavelength separation of 30%. The results are shown in Fig. 5(ii). PaCMAN without monochromatization still has better performance for all wavelengths compared to ePIE, but the two algorithms converge to similar error at high fluxes (Fig. 5(iia,b,d)). Monochromatization with CGLS provides worse

Optics EXPRESS

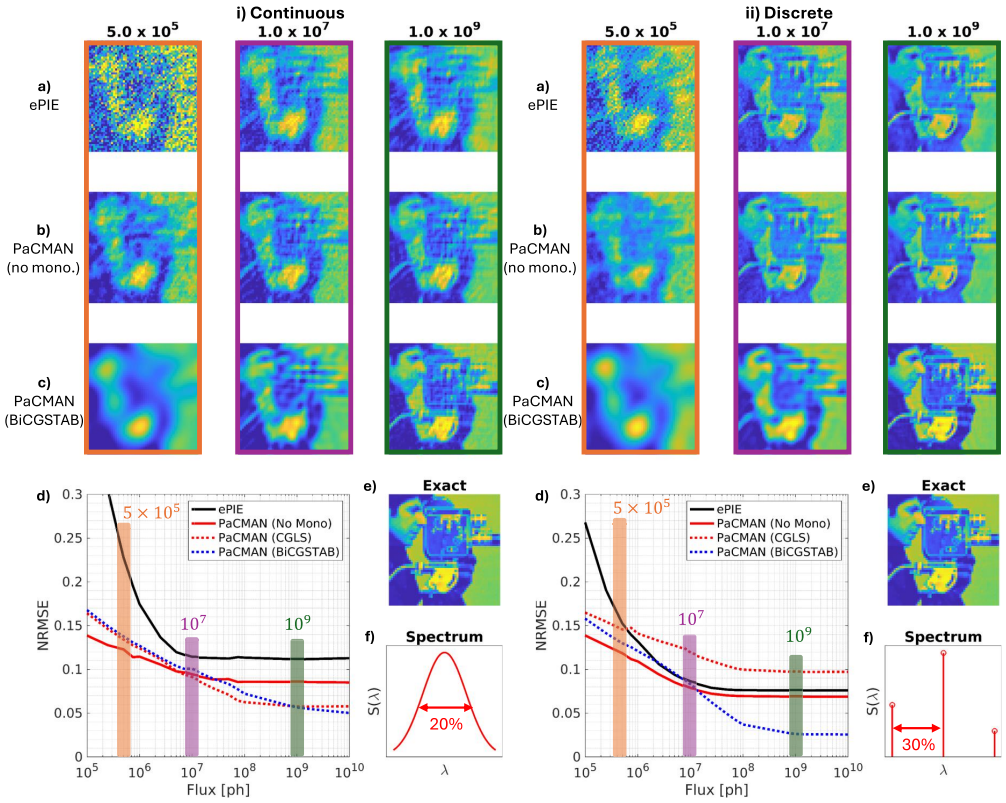

Fig. 5. Comparison between ePIE and PaCMAN for i) a continuous spectrum and ii) a discrete spectrum. a) The reconstructed object modulus from a) ePIE, b) PaCMAN without monochromatization, and c) PaCMAN with monochromatization using BiCGSTAB. Each column corresponds to a different flux. d) NRMSE vs. flux incident on the target for ePIE and PaCMAN. e) Exact object modulus for comparison. f) Spectrum used.

reconstruction quality across all fluxes, while BiCGSTAB provides significant improvement for fluxes above 10^7. Thus, PaCMAN can achieve excellent reconstructions even for discrete spectra contaminated by noise and artifacts.

4.4. *Varying probe overlap to test dose reduction*

Assuming a constant flux from the source, the total dose applied to the sample will be proportional to the camera integration time, so reducing the dose needed to achieve a desired resolution will accelerate data acquisition. Moreover, for radiation sensitive materials like polymers or biological cells, reducing the dose applied is crucial for preventing damage [31].

For a constant photon count per scan position, the dose D applied to the target can be expressed in terms of the linear probe overlap O and size of the diffraction patterns M_{dp} as

$$D \propto \frac{1}{(1-O)^2} \propto M_{\mathrm{dp}}. \tag{23}$$

Dose is proportional to the scan density s^{-2}, where $s = 2R_{\mathrm{prb}}(1-O)$ is the separation between scan positions for a given probe radius R_{prb}. Thus, dose is proportional $(1-O)^{-2}$. Note that in estimating dose, we are also assuming that the absorbed dose is wavelength-independent over the illumination bandwidth.

Optics EXPRESS

From our results varying the flux (Fig. 5(id)), a photon count of 10^9 is where the NRMSE reaches its minimum value for both PaCMAN and ePIE, so in this section we set the photon count to 10^9. We enable Gaussian and Poisson noise, but not parasitic scattering. We then vary O from 0.3 to 0.9, which corresponds to a dose range of 2 to 100 (in arbitrary units). We examine the performance of ePIE, PaCMAN without monochromatization, and PaCMAN with monochromatization. In theory (and as confirmed by Fig. 4(i)), monochromatic sources always achieve higher resolution than quasi-monochromatic sources at the same dose, as ptychography algorithms assume monochromatic illumination. However, in practice, the need for femtosecond/attosecond pulses, lack of effective monochromatizing optics, or speed increase from higher total flux necessitate broader bandwidths. To comprehensively analyze dose efficiency, we simulate bandwidths of 1%, 5%, 10%, and 20%. We perform 300 iterations for each algorithm, with step sizes for the probe/object in ePIE set to 0.7 and $r = 0.4$ for PaCMAN.

Our results are shown in Fig. 6. Examining the NRMSE plots (Fig. 6(a-d)), we find that decreasing the bandwidth decreases the dose required to achieve a desired NRMSE, as expected. Regardless of bandwidth, PaCMAN without monochromatization reduces the dose relative to ePIE. With monochromatization, PaCMAN becomes even more efficient, most notably at larger bandwidths. The total dose reduction from PaCMAN ranges from 1.5-25x within each bandwidth. For example, for a bandwidth of 10%, PaCMAN with monochromatization at $O = 0.5$ (Fig. 6(j3)) has the same NRMSE as ePIE at $O = 0.9$ (Fig. 6(i1)) while having 25x lower dose. At a bandwidth of 20%, PaCMAN with monochromatization at $O = 0.5$ (Fig. 6(l3)) has a lower NRMSE than ePIE at $O = 0.9$ (Fig. 6(k1)) while having more than 25x lower dose. As we approach a monochromatic illumination with 1% bandwidth, each algorithm converges to the exact object at high overlaps, although PaCMAN still provides a modest dose reduction of about 1.5-2x at small overlaps. Increasing the number of iterations from 300 to 1000 does not significantly change the results, and from testing lower contrast objects, we saw similar improvement of PaCMAN relative to ePIE, though both algorithms had lower performance.

One surprising result from comparing Fig. 6(a) and 6(c) is that PaCMAN with monochromatization at 10% achieves a low NRMSE of 0.05 at $D \approx 3.2$, while ePIE at 1% achieves the same NRMSE at $D \approx 4.8$. This means that even at broad bandwidths, PaCMAN is more dose-efficient than ePIE with nearly monochromatic illumination.

4.5. Ms. PaCMAN

As a proof of concept, we compared Ms. PaCMAN without any additional spatial modes to Ptychographic Information Multiplexing (PIM) [13] for the same continuous and discrete spectra used in the flux section. We assumed that the object and probes were the same for each wavelength. Since each wavelength has a different pixel size in the object plane, we scaled the probes and objects to maintain the same physical size for each wavelength. We applied noise and parasitic scatting to each diffraction pattern.

For the continuous Gaussian spectrum with a bandwidth of 20%, we used nine uniformly sampled wavelengths for both PIM and Ms. PaCMAN. The reconstructed objects and errors for the center wavelength are shown in Fig. 7(i). When we compare PIM (Fig. 7(ia), flux of 10^9) to ePIE (Fig. 5(ia), flux of 10^9), we achieve a lower NRMSE, with more distinguishable features in the image. However, compared to PaCMAN, PIM has higher NRMSE for all fluxes (Fig. 7(ic)). Monochromatization still achieves a lower NRMSE error (Fig. 5(ic)), which can be clearly seen in the sharp features of Fig. 5(ic) relative to Fig. 7(ib) at a flux of 10^9. We also plot the five central wavelength reconstructions from PIM and Ms. PaCMAN in Fig. 8, where we see a slight improvement in image quality from Ms. PaCMAN.

For the discrete three-wavelength spectrum with a separation of 30%, we used three wavelengths in PIM and Ms. PaCMAN. The results are shown in Fig. 7(ii). Both PIM and Ms. PaCMAN give excellent reconstructions at high fluxes of 10^8 or higher, with Ms. PaCMAN having lower

Optics EXPRESS

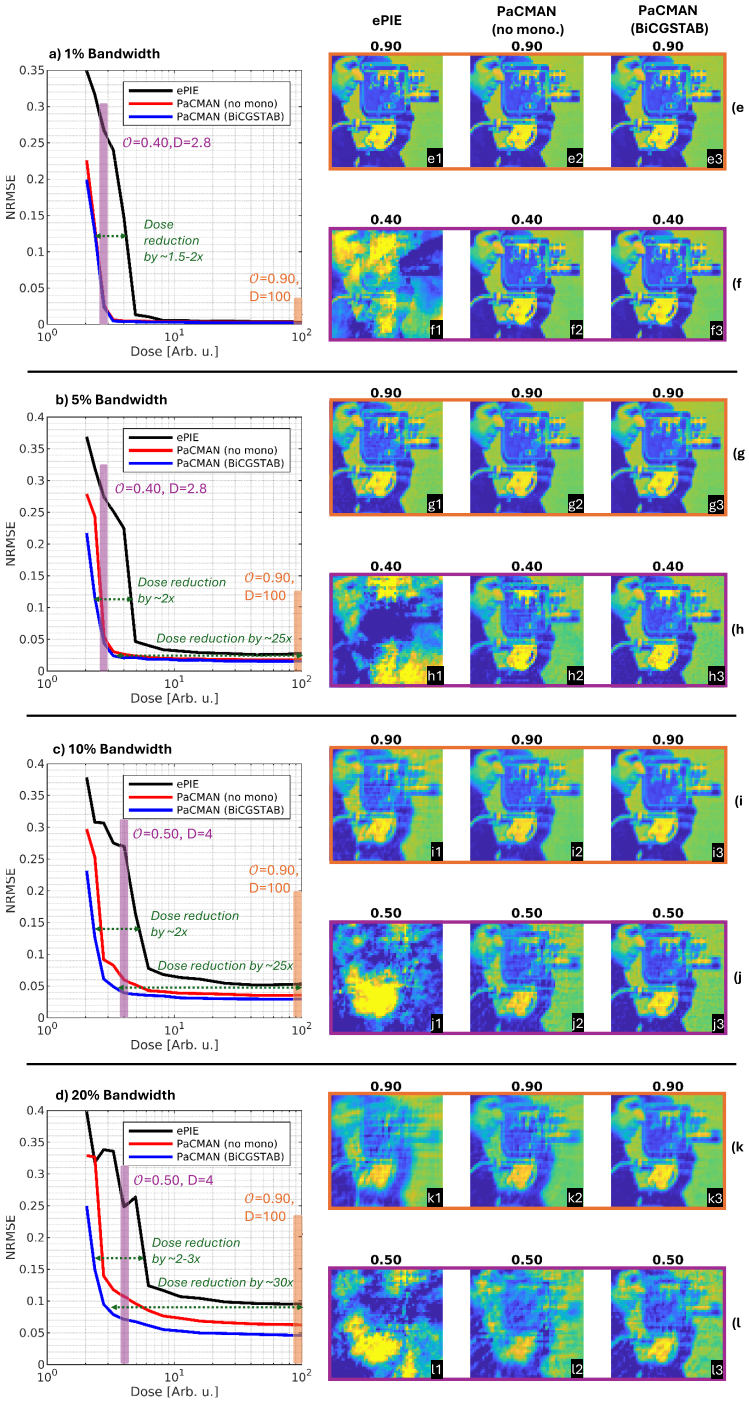

Fig. 6. Comparison between ePIE and PaCMAN for probe overlaps of 0.3 to 0.9, or equivalently doses of 2 to 100. a-d) Plot of NRMSE vs. dose for each bandwidth. e-l) Plot of the reconstructed object modulus, with column 1 for ePIE, col. 2 for PaCMAN (no monochromatization), and col. 3 for PaCMAN (with monochromatization).

Optics EXPRESS

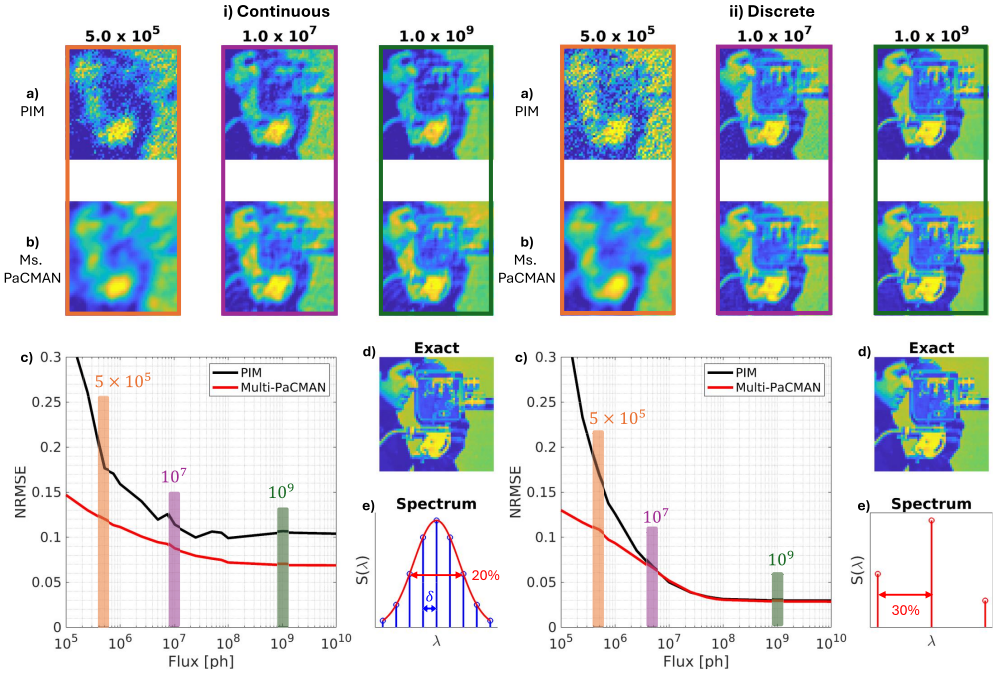

Fig. 7. Comparison between PIM and Ms. PaCMAN for i) a continuous spectrum and ii) a discrete spectrum. a) The reconstructed object modulus from PIM for a given flux incident on the sample. b) The reconstructed object modulus from Ms. PaCMAN. c) NRMSE vs. flux incident on the target for PIM and multi-wavelength PaCMAN. d) Exact object modulus for comparison. e) Spectrum used. For the continuous case, the nine reconstructed wavelengths are indicated by the blue delta functions.

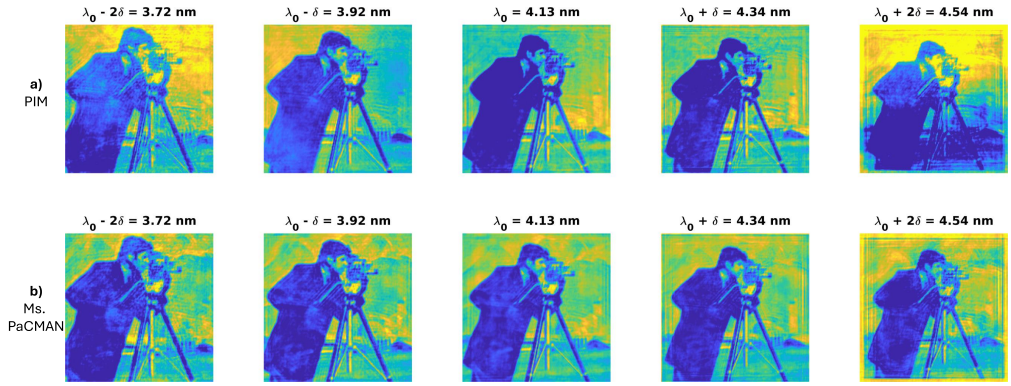

Fig. 8. Object modulus reconstructed by a) PIM and b) Ms. PaCMAN for the central five wavelengths.

Optics EXPRESS

NRMSE at low fluxes. By comparing Fig. 5(ii) and Fig. 7(ii), we can see that for this discrete spectrum, monochromatization and multi-wavelength algorithms give comparable results.

4.6. Memory costs and runtime

Understanding the hardware requirements for ePIE and PaCMAN is important for their practical usage. ePIE is a serial method: within each iteration, we loop through each position and update the probe and object, resulting in a low memory cost. PaCMAN is a parallel method: within each iteration, the entire object and probe can be updated simultaneously without looping through positions, resulting in a high memory cost.

M_{ePIE}, the memory usage of ePIE, is approximately equal to the memory required to store the diffraction patterns M_{dp}. For PaCMAN, when we account for all the variables and N_M additional modes, the memory requirement is

$$M_{\mathrm{PaCMAN}} \approx (14 + 10N_M)M_{\mathrm{dp}} \approx (14 + 10N_M)M_{\mathrm{ePIE}}, \tag{24}$$

more than ten times that of ePIE. For the data acquired in Fig. 5, ePIE had a total GPU memory requirement of 0.089 GB while PaCMAN with $N_M = 2$ (with or without monochromatization) had a total memory GPU requirement of 3.0 GB for $256 \times 256 \times 169$ double precision (89 MB) diffraction patterns. Both of these can easily fit in a single one of our 40 GB NVIDIA A100 GPUs.

For Ms. PaCMAN, $N_M = N_{sp}(N_w - 1)$, where N_{sp} is the number of spatial modes and N_w the number of wavelengths. For continuous spectra, we may need N_w>10, making Ms. PaCMAN roughly an order of magnitude more memory intensive than PaCMAN.

Despite the increase in memory, the iterative portion of PaCMAN has a runtime comparable to ePIE. For the data acquired in Fig. 5 (100 iterations), ePIE had a runtime of 15 seconds while PaCMAN (without monochromatization) had a runtime of 25 seconds. The monochromatization step adds a few extra seconds. Without the two additional spatial modes and monochromatization, PaCMAN has a runtime of 17 seconds. While not extensively tested here, we have found that PaCMAN has a faster convergence than ePIE in the presence of artifacts, thus requiring fewer iterations overall. We also note that since dose is proportional to the size of the diffraction patterns (Eq. (23)) and PaCMAN achieves the same NRMSE as ePIE with 1.5-25x lower dose, the total memory cost for PaCMAN could be only a few times larger than ePIE, with each iteration running faster than ePIE. This is especially important for the more computationally demanding Ms. PaCMAN. Calculating C took a few minutes when using parallelized CPU processing, but is only calculated once per spectrum.

5. Discussion

From the noiseless monochromatization results, we found that BiCGSTAB and CGLS give comparable improvements at bandwidths below 10% regardless of spectrum. For continuous Gaussian spectra (Fig. 4(i)), BiCGSTAB provides a moderate decrease in the error relative to CGLS for reconstructions above 10% bandwidth. For a given NRMSE, monochromatization with BiCGSTAB provides the same error at more than twice the bandwidth, which means that we can extend usable flux by more than a factor of two without changing the NRMSE.

We then fixed the bandwidth to 20% and enabled noise (Fig. 5(i)) to compare ePIE to PaCMAN for different fluxes, finding that PaCMAN can give high quality reconstructions at high fluxes despite the large bandwidth, parasitic scattering, and noise. ePIE, on the other hand, cannot. We note that the monochromatization step is sensitive to noise, which means it is only useful for fluxes greater than 10^7, or a mean of 7×10^6 photons in each diffraction pattern for our chosen sample transmission. In practice, for continuous spectra, CGLS and BiCGSTAB are interchangeable: CGLS provides lower error at moderate fluxes, while BiCGSTAB provides lower error at high fluxes.

Optics EXPRESS

By varying probe overlap (Fig. 6), we found that the iterative core of PaCMAN is more dose-efficient than ePIE, owing to the more robust ADMM framework of PaCMAN. With monochromatization, it is even more robust, providing a 1.5-25x decrease in the dose required. Smaller bandwidths are intrinsically more dose efficient, which means that the smallest feasible bandwidth should be chosen for the radiation-sensitive experiments. For 1% bandwidths, PaCMAN can achieve excellent reconstructions at 1.5-2x lower dose than ePIE. This could be especially important in minimizing the vast data required for spectro-ptycho-tomography experiments, which involve scanning a small bandwidth probe in photon energy (spectroscopy), position (ptychography), and angle (tomography) [12]. Low-dose non-iterative approaches based on machine learning have also been demonstrated that are capable of achieving fair reconstruction quality at probe overlaps approaching zero by stitching together predicted object transmissions [32,33]. These approaches likely outperform PaCMAN at very small overlaps, though integrating machine learning with PaCMAN to improve its performance at low probe overlaps could be a powerful way to further reduce dose. More studies should also be conducted to see if the dose reduction of ADMM over ePIE by reducing probe overlap also holds compared to other algorithms such as LSQ-ML [34], sDR [35], or automatic differentiation [36].

If speed rather than dose efficiency is the top priority, then a bandwidth of about 10% seems to be ideal for PaCMAN, while for ePIE it is about 5%. Comparing both algorithms for reasonably low NRMSE of 0.05, PaCMAN will enable about 4x faster data acquisition than speed-optimized ePIE due to twice the flux and about 1/2 the dose. This will be useful for sub-10 nm imaging with table-top SXR HHG sources [27] or ptycho-tomography with large data-sets. While not rigorously demonstrated here, we have found that the improvements in speed and dose reduction are comparable when we reduce the object contrast, which is relevant for optically thick samples in the SXR. A promising avenue for future work will be combining this algorithm with strong reference scatterers placed in the sample plane or in a plane slightly in front of the sample, which could provide an additional order of magnitude decrease in dose [37,38].

Next, we demonstrated Ms. PaCMAN, which is the first multi-wavelength algorithm based on the general ADMM framework that includes parasitic scattering. When we ran Ms. PaCMAN on the same continuous 20% spectrum as Fig. 5(i), we were able to reduce the error relative to PaCMAN without monochromatization, but the reconstruction was not as good as PaCMAN with monochromatization (Fig. 7(i)). This reinforces that monochromatization is better than multi-wavelength algorithms for continuous spectra of moderate bandwidths around 20% (see Fig. 9). However, like PaCMAN compared to ePIE, when we compared Ms. PaCMAN to PIM, we found that it had superior performance at all fluxes. In other work, a method called Spectrum, Probe, and Image REconstruction (SPIRE) improved upon PIM by including additional spatial modes and probe replacement, allowing more wavelengths to be reconstructed at high quality [11]. By enabling multiple spatial modes and adding probe replacement to Ms. PaCMAN, we expect that it can surpass SPIRE's performance. Future work will explore how Ms. PaCMAN compares to SPIRE when the probes and objects are wavelength dependent, and test to see how much Ms. PaCMAN can reduce the dose to get the same image quality.

In addition to continuous Gaussian spectra, we also tested the monochromatization and multi-wavelength algorithms on a discrete three-wavelength spectrum. For the high flux case, we found that BiCGSTAB gives near perfect reconstructions regardless of the separation between the wavelengths, while CGLS is only effective for small separations (Fig. 4(ii)). This is the first demonstration of a monochromatization algorithm for discrete spectra. After we tested it with noise (Fig. 5(ii)), we compared it to Ms. PaCMAN and PIM(Fig. 7(ii)), finding that we get excellent reconstruction quality from both PaCMAN and Ms. PaCMAN. Thus, for EUV HHG sources that emit a comb of harmonics, monochromatization is a viable alternative for making use of (or correcting for) multiple harmonics (see Fig. 9), provided the objects/probes are approximately wavelength independent. Monochromatization could potentially be combined

Optics EXPRESS

Do we know the spectrum? (from a spectrometer, pulse characterization method, etc.)	**Are the probes/objects λ-independent?** (achromatic optics, no abs. edges, etc.)	**Algorithm(s) to use**	**Algorithm Constraints**	**Data Required for Discrete Spectrum (Probe Overlap)**	**Data Required for Continuous Spectrum (Probe Overlap)**
No	Yes	Multi-wavelength	None	Large	Very large
No	No	Multi-wavelength	Object/Probe Scaling	Moderate	Large
Yes	No	Multi-wavelength	Spectrum	Moderate	Large
Yes	Yes	Multi-wavelength Monochromatization	Spectrum and Object/Probe Scaling	Small Small	Moderate Small

Priority	Optimized Algorithms	Improvement of PaCMAN over ePIE	Applications
Speed (More flux/less data)	ePIE, ~5% bw PaCMAN, ~10% bw	~4x speed (2x flux, ½ data)	SXR HHG, ptycho-tomography (big datasets)
Dose (Less scans)	ePIE, ~1% bw PaCMAN, ~1% bw	1.5-2x lower dose	Radiation sensitive samples, energy-scanned spectro-ptychography

Fig. 9. Table for selecting an algorithm for broadband correction. Monochromatization is the most heavily constrained algorithm, which means less data is required to get excellent reconstructions. Multi-wavelength algorithms with an unknown spectrum and wavelength dependent probes/objects require significantly more data to converge because they are poorly constrained. A summary comparing PaCMAN and ePIE optimized for speed and dose are shown below the table.

with spatial entropy engineering to ensure wavelength-independent illumination within a desired bandwidth [39].

The last variables of importance when deciding which bandwidth to use are geometrical parameters. For the spectral blurring caused by broadband illumination to be negligible, we require the probe radius to satisfy [40,41]

$$R < \frac{\lambda^2}{2\Delta\lambda \sin(\alpha)} \approx \frac{z\lambda^2}{\Delta\lambda N d s}. \tag{25}$$

With our simulated setup, the max angle at which we get usable signal is $\sin(\alpha) \approx Nds/z$, the object-detector distance is $z = 5$ cm, the center wavelength is $\lambda = 4.13$ nm, the probe radius is $R = 0.608$ μm, effective detector pixel size is $ds = 40$ μm, and the pixel dimension of the detector is $N = 256$. This means that for relative bandwidths

$$\frac{\Delta\lambda}{\lambda} < \frac{z\lambda}{RNds} = 3.12\%, \tag{26}$$

the illumination is effectively monochromatic, which agrees well with our results: ePIE performs very well for 1% and even 5%, but sharply drops in performance at 10% and higher. For our selected parameters, the limit at which PaCMAN can achieve excellent reconstructions seems to be about 20% bandwidth (Fig. 6(d)). By reducing the probe size further, or by increasing the divergence of the probe [42], we may be able to extend monochromatization to even larger bandwidths. Alternatively, increasing object-detector distance should also benefit reconstructions at larger bandwidths (albeit at the expense of resolution), as suggested by Huijt's *et al.* [10] and Eq. (26). We hypothesize that the bandwidth results of our simulation study will scale linearly

Optics EXPRESS

with Eq. (26), e.g. if we double z, we may be able to get excellent reconstructions up to 40% bandwidth. Not accounting for the effective monochromaticity or the fact that ptychography is more robust to bandwidth than single-shot CDI is a likely cause of discrepancies between the maximum bandwidths of monochromatization algorithms cited in the literature, e.g. about 11% for CDI in [10], about 15.8% for ptychography in [18], about 20% for ptychography in this manuscript, and about 40% for ptychography in [19]. Future simulations and experiments will seek to verify this.

Overall, PaCMAN is a more efficient algorithm than ePIE in nearly every case except when ultra-narrow bandwidths with near-perfect reconstruction quality are required. This comes at the expense of roughly an order of magnitude higher memory costs. However, since the monochromatization step is separate from the iterative part of PaCMAN, our monochromatization results can be readily applied to ePIE, other ptychography algorithms, or CDI more generally. Future work will explore how the monochromatization and multi-wavelength components can be combined to improve performance relative to either algorithm alone, and how machine learning could be combined with PaCMAN to further reduce probe overlap and therefore dose.

6. Conclusion

In summary, we introduced PaCMAN and Ms. PaCMAN to account for partial spatial coherence, shot noise, parasitic scattering, and broad bandwidth illumination. By improving the monochromatization algorithm, we demonstrated superior performance at continuous bandwidths at low noise levels and significantly better performance for discrete spectra. We showed that the iterative portion of PaCMAN can provide a substantial improvement over ePIE when the diffraction patterns have noise and artifacts, while the monochromatization step provides a further increase for broadband illumination beyond a flux of 10^7 photons. PaCMAN can recover images with a quality comparable to ePIE at 1.5-2x lower dose, allowing imaging of radiation sensitive samples without causing damage. When both algorithms are optimized for speed, PaCMAN is still about four times faster than ePIE, as the usable flux is doubled while the rigorous ADMM framework allows half the scan positions to be used, which will allow rapid imaging using future SXR HHG sources. Finally, we show how Ms. PaCMAN outperforms multi-wavelength algorithms based on ePIE, enabling attosecond CDI at lower doses. Ultimately, these algorithms will advance attoscience, low-dose imaging, and attempts to achieve sub-10 nm with SXR HHG sources.

Funding. Multidisciplinary University Research Initiative (FA9550-23-1-0281); Gordon and Betty Moore Foundation (10784); STROBE National Science Foundation Science & Technology Center (DMR-1548924).

Acknowledgments. The authors gratefully acknowledge funding for this work from the Gordon and Betty Moore Foundation Grant No. 10784 for the hyper spectral imaging research, from an U.S. Air Force Office Multidisciplinary University Research Initiative (MURI) program under award no. 487 FA9550-23-1-0281 for the low-dose imaging research imaging technique, and from the STROBE National Science Foundation Science & Technology Center, Grant No. DMR-1548924, for the skyrmion imaging data. We also thank Sadegh Yazdi for acquiring the SEM image of our Fe/Gd sample used in the ptycho-tomography experiments.

Disclosures. The authors declare no conflicts of interest.

Data availability. The MATLAB code for PaCMAN and Ms. PaCMAN can be downloaded from [43]. The data underlying the results presented in this paper are not publicly available at this time but may be obtained from the authors upon reasonable request.

References

1. D. F. Gardner, M. Tanksalvala, E. R. Shanblatt, *et al.*, "Subwavelength coherent imaging of periodic samples using a 13.5 nm tabletop high-harmonic light source," Nat. Photonics **11**(4), 259–263 (2017).
2. L. Loetgering, S. Witte, and J. Rothhardt, "Advances in laboratory-scale ptychography using high harmonic sources," Opt. Express **30**(3), 4133–4164 (2022).
3. R. Khubbutdinov, A. P. Menushenkov, and I. A. Vartanyants, "Coherence properties of the high-energy fourth-generation X-ray synchrotron sources," J. Synchrotron Radiat. **26**(6), 1851–1862 (2019).
4. R. A. Bartels, A. Paul, H. Green, *et al.*, "Generation of spatially coherent light at extreme ultraviolet wavelengths," Science **297**(5580), 376–378 (2002).

Optics EXPRESS

5. H. Chang, P. Enfedaque, J. Zhang, *et al.*, "Advanced denoising for x-ray ptychography," Opt. Express **27**(8), 10395–10418 (2019).
6. P. Thibault and A. Menzel, "Reconstructing state mixtures from diffraction measurements," Nature **494**(7435), 68–71 (2013).
7. T. Popmintchev, M.-C. Chen, D. Popmintchev, *et al.*, "Bright coherent ultrahigh harmonics in the kev x-ray regime from mid-infrared femtosecond lasers," Science **336**(6086), 1287–1291 (2012).
8. D. Popmintchev, B. R. Galloway, M.-C. Chen, *et al.*, "Near-and extended-edge x-ray-absorption fine-structure spectroscopy using ultrafast coherent high-order harmonic supercontinua," Phys. Rev. Lett. **120**(9), 093002 (2018).
9. R. L. Sandberg, A. Paul, D. A. Raymondson, *et al.*, "Lensless diffractive imaging using tabletop coherent high-harmonic soft-x-ray beams," Phys. Rev. Lett. **99**(9), 098103 (2007).
10. J. Huijts, S. Fernandez, D. Gauthier, *et al.*, "Broadband coherent diffractive imaging," Nat. Photonics **14**(10), 618–622 (2020).
11. A. Rana, J. Zhang, M. Pham, *et al.*, "Potential of attosecond coherent diffractive imaging," Phys. Rev. Lett. **125**(8), 086101 (2020).
12. S. G. Urquhart, "X-ray spectroptychography," ACS Omega **7**(14), 11521–11529 (2022).
13. D. J. Batey, D. Claus, and J. M. Rodenburg, "Information multiplexing in ptychography," Ultramicroscopy **138**, 13–21 (2014).
14. B. Abbey, L. W. Whitehead, H. M. Quiney, *et al.*, "Lensless imaging using broadband x-ray sources," Nat. Photonics **5**(7), 420–424 (2011).
15. B. Zhang, D. F. Gardner, M. H. Seaberg, *et al.*, "Ptychographic hyperspectral spectromicroscopy with an extreme ultraviolet high harmonic comb," Opt. Express **24**(16), 18745–18754 (2016).
16. M. Du, X. Liu, A. Pelekanidis, *et al.*, "High-resolution wavefront sensing and aberration analysis of multi-spectral extreme ultraviolet beams," Optica **10**(2), 255–263 (2023).
17. B. Enders, "Development and application of decoherence models in ptychographic diffraction imaging," Ph.D. thesis, Technische Universität München (2016).
18. R. Liu, W. Cao, Q. You, *et al.*, "Broadband ptychographic imaging with an accurately sampled spectrum," Phys. Rev. A **107**(3), 033510 (2023).
19. C. Chen, H. Gu, and S. Liu, "Ultra-broadband diffractive imaging with unknown probe spectrum," Light: Sci. Appl. **13**(1), 213 (2024).
20. C. Chen, H. Gu, and S. Liu, "Ultra-simplified diffraction-based computational spectrometer," Light: Sci. Appl. **13**(1), 9 (2024).
21. P. Thibault and M. Guizar-Sicairos, "Maximum-likelihood refinement for coherent diffractive imaging," New J. Phys. **14**(6), 063004 (2012).
22. H. Chang, P. Enfedaque, and S. Marchesini, "Blind ptychographic phase retrieval via convergent alternating direction method of multipliers," SIAM J. Imaging Sci. **12**(1), 153–185 (2019).
23. H. Yan, "Ptychographic phase retrieval by proximal algorithms," New J. Phys. **22**(2), 023035 (2020).
24. L. Loetgering, M. Du, D. Boonzajer Flaes, *et al.*, "Ptylab. m/py/jl: a cross-platform, open-source inverse modeling toolbox for conventional and fourier ptychography," Opt. Express **31**(9), 13763–13797 (2023).
25. K. Wakonig, H.-C. Stadler, M. Odstrčil, *et al.*, "Ptychoshelves, a versatile high-level framework for high-performance analysis of ptychographic data," J. Appl. Crystallogr. **53**(2), 574–586 (2020).
26. A. M. Maiden and J. M. Rodenburg, "An improved ptychographical phase retrieval algorithm for diffractive imaging," Ultramicroscopy **109**(10), 1256–1262 (2009).
27. W. Hettel, G. Golba, D. Morrill, *et al.*, "Compact, ultrastable, high repetition-rate 2 μm and 3 μm fiber laser for seeding mid-ir opcpa," Opt. Express **32**(3), 4072–4080 (2024).
28. J. Huijts, "Broadband coherent x-ray diffractive imaging and developments towards a high repetition rate mid-ir driven kev high harmonic source," Ph.D. thesis, Université Paris Saclay (COmUE) (2019).
29. H. A. Van der Vorst, "Bi-cgstab: A fast and smoothly converging variant of bi-cg for the solution of nonsymmetric linear systems," SIAM J. Sci. and Stat. Comput. **13**(2), 631–644 (1992).
30. O. Bunk, M. Dierolf, S. Kynde, *et al.*, "Influence of the overlap parameter on the convergence of the ptychographical iterative engine," Ultramicroscopy **108**(5), 481–487 (2008).
31. M. R. Howells, T. Beetz, H. N. Chapman, *et al.*, "An assessment of the resolution limitation due to radiation-damage in x-ray diffraction microscopy," J. Electron Spectrosc. Relat. Phenom. **170**(1-3), 4–12 (2009).
32. M. J. Cherukara, T. Zhou, Y. Nashed, *et al.*, "Ai-enabled high-resolution scanning coherent diffraction imaging," Appl. Phys. Lett. **117**(4), 044103 (2020).
33. A. V. Babu, T. Zhou, S. Kandel, *et al.*, "Deep learning at the edge enables real-time streaming ptychographic imaging," Nat. Commun. **14**(1), 7059 (2023).
34. M. Odstrčil, A. Menzel, and M. Guizar-Sicairos, "Iterative least-squares solver for generalized maximum-likelihood ptychography," Opt. Express **26**(3), 3108–3123 (2018).
35. M. Pham, A. Rana, J. Miao, *et al.*, "Semi-implicit relaxed douglas-rachford algorithm (sdr) for ptychography," Opt. Express **27**(22), 31246–31260 (2019).
36. L. Wu, S. Yoo, Y. S. Chu, *et al.*, "Dose-efficient automatic differentiation for ptychographic reconstruction," Optica **11**(6), 821–830 (2024).

Optics EXPRESS

37. Y. H. Lo, L. Zhao, M. Gallagher-Jones, *et al.*, "In situ coherent diffractive imaging," Nat. Commun. **9**(1), 1826 (2018).
38. C. Kim, Y. Kim, C. Song, *et al.*, "Enhancing resolution in coherent x-ray diffraction imaging," J. Phys.: Condens. Matter **28**(49), 493001 (2016).
39. L. Loetgering, X. Liu, A. C. De Beurs, *et al.*, "Tailoring spatial entropy in extreme ultraviolet focused beams for multispectral ptychography," Optica **8**(2), 130–138 (2021).
40. F. Van der Veen and F. Pfeiffer, "Coherent x-ray scattering," J. Phys.: Condens. Matter **16**(28), 5003–5030 (2004).
41. B. Enders, M. Dierolf, P. Cloetens, *et al.*, "Ptychography with broad-bandwidth radiation," Appl. Phys. Lett. **104**(17), 171104 (2014).
42. D. S. Penagos Molina, L. Loetgering, W. Eschen, *et al.*, "Broadband ptychography using curved wavefront illumination," Opt. Express **31**(16), 26958–26968 (2023).
43. B. Shearer, H. Kapteyn, I. Binni, *et al.*, "Robust broadband ptychography algorithms for high-harmonic soft X-ray supercontinua: code," Github, 2024, https://github.com/besh5711/PaCMAN